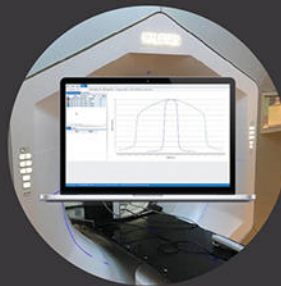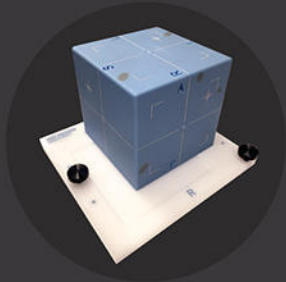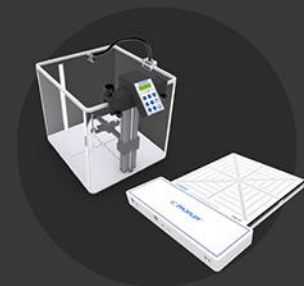# Solutions Spotlight

NEW! PlanCHECK™
Automated plan quality verification and reporting – available as part of the SunCHECK™ Platform

Varian Halcyon™ System Support
SNC Dosimetry™ v3.6 and 3D SCANNER™ for beam model verification and Halcyon Package for acceptance and verification

NEW! MultiPHAN™
An easy-to-use tool for comprehensive TG-142 daily alignment checks – verifying lasers to EPIDs to CBCT systems

Stereotactic Solutions
NEW SRS MapCHECK™ and StereoPHAN™ for end-to-end testing and Reference Detector for interference-free dosimetry scanning

MR-Based Radiotherapy
Custom patient and machine QA solutions, including ArcCHECK®-MR, IC PROFILER™-MR, MICRO+™ MR, and Solid Water® HE

See more. Learn more.
sunnuclear.com

SUN NUCLEAR corporation

Flexible mini gamma camera reconstructions of extended sources using step and shoot and list mode

José Gardiazabal
Department of Informatics, Technische Universität München, München 80333, Germany and Klinikum Rechts der Isar, Technische Universität München, München 80333, Germany

Philipp Matthies, Jakob Vogel,[a)] and Benjamin Frisch
Department of Informatics, Technische Universität München, München 80333, Germany

Nassir Navab
School of Engineering, Johns Hopkins University, Baltimore, Maryland 21218 and Department of Informatics, Technische Universität München, München 80333, Germany

Sibylle Ziegler
Klinikum Rechts der Isar, Technische Universität München, München, München 80333,Germany

Tobias Lasser[b)]
Department of Informatics, Technische Universität München, München 80333, Germany

Purpose: Hand- and robot-guided mini gamma cameras have been introduced for the acquisition of single-photon emission computed tomography (SPECT) images. Less cumbersome than whole-body scanners, they allow for a fast acquisition of the radioactivity distribution, for example, to differentiate cancerous from hormonally hyperactive lesions inside the thyroid. This work compares acquisition protocols and reconstruction algorithms in an attempt to identify the most suitable approach for fast acquisition and efficient image reconstruction, suitable for localization of extended sources, such as lesions inside the thyroid.

Methods: Our setup consists of a mini gamma camera with precise tracking information provided by a robotic arm, which also provides reproducible positioning for our experiments. Based on a realistic phantom of the thyroid including hot and cold nodules as well as background radioactivity, the authors compare "step and shoot" (SAS) and continuous data (CD) acquisition protocols in combination with two different statistical reconstruction methods: maximum-likelihood expectation–maximization (ML-EM) for time-integrated count values and list-mode expectation–maximization (LM-EM) for individually detected gamma rays. In addition, the authors simulate lower uptake values by statistically subsampling the experimental data in order to study the behavior of their approach without changing other aspects of the acquired data.

Results: All compared methods yield suitable results, resolving the hot nodules and the cold nodule from the background. However, the CD acquisition is twice as fast as the SAS acquisition, while yielding better coverage of the thyroid phantom, resulting in qualitatively more accurate reconstructions of the isthmus between the lobes. For CD acquisitions, the LM-EM reconstruction method is preferable, as it yields comparable image quality to ML-EM at significantly higher speeds, on average by an order of magnitude.

Conclusions: This work identifies CD acquisition protocols combined with LM-EM reconstruction as a prime candidate for the wider introduction of SPECT imaging with flexible mini gamma cameras in the clinical practice. *© 2016 Author(s). All article content, except where otherwise noted, is licensed under a Creative Commons Attribution (CC BY) license (http://creativecommons.org/licenses/by/4.0/).* [http://dx.doi.org/10.1118/1.4966700]

Key words: Image reconstruction, medical imaging, single photon emission computed tomography, list-mode

1. INTRODUCTION

Thyroid cancer occurrence has doubled since 1993 in the United Kingdom, with 2500 cases in 2012 and 53 000 cases within Europe.[1] A similar trend can be observed in many other countries, and the reasons for the increase appear to be unclear.[2,3] It has been suggested that both incidental detection during ultrasound examinations as well as risk factors such as radiation exposure and obesity might be among the causes.[4] Similar to other cancers, survival chances depend largely on quick and accurate staging and stratification.[5]

For the tumor localization inside the thyroid in subnormal thyroid-stimulating hormone (TSH) patients, a radionuclide scan is strongly recommended.[6] A suitable biochemical agent, marked with a radioactive element ("tracer") emitting gamma-rays such as ^{99m}Tc, is employed. For example, sodium

pertechnetate ($Na^{99m}TcO_4$) is injected into the patient, since it behaves similar to iodine and concentrates in the parenchymal regions of the thyroid.[7] The uptake in the different regions of the thyroid is correlated to the hormone production, that means regions with higher hormone production absorb more pertechnetate, whereas the cancerous regions, that have high growth but no hormone production, tend not to accumulate it.

To produce a planar image of the radioactivity distribution, which corresponds to the labeled regions, a gamma camera detects gamma rays produced in the respective cone-shaped fields of view of the individual sensors. Such an image can be considered a two-dimensional projection of a structure in three-dimensional space. Several studies have shown that volumetric visualization based on single-photon emission computed tomography (SPECT) leads to better performance for thyroid cases.[8,9]

Since the thyroid is a rather small organ located close to the surface of the neck, instead of a whole-body SPECT scanner, it is promising to use a tracked miniaturized gamma-detector to collect radiation measurements in close proximity and to perform a tomographic reconstruction. This approach has been implemented both using a hand-guided, optically tracked single detector such as is used for radio-guided surgery,[10,11] as well as a robot-mounted mini gamma camera, as a stand-alone device[12] or in combination with a C-arm computed tomography scanner.[13] These systems have demonstrated that radioactive hot spots, such as small spheres resembling metastatic lymph nodes, can be localized with high precision, delivering image quality close to that of regular SPECT devices. So far these studies restricted themselves to "hot" regions with limited or no background radiation, which is realistic to assume for lymph nodes, localized metastases, or the targeted injection of radioactivity, but not for the thyroid case at hand.

In addition, those systems rely on binned-mode data reconstruction algorithms (Maximum-Likelihood Expectation–Maximization, or ML-EM in short), using time-integrated count values. It has been shown[14,15] that using list-mode data reconstruction algorithms (List-Mode Expectation–Maximization or LM-EM in short) can yield improved results, as it allows the usage of more precise information, such as the exact point of interaction or the energy of each detected photon. In fact, list-mode data processing allows for novel analytic reconstruction formulas; for an overview we refer the reader to the work of Jha *et al.*[15]

In this work, we investigate acquisition and reconstruction strategies for nuclear imaging using a robotically controlled and tracked mini gamma camera with a parallel hole collimator detecting individual gamma rays, considering the application scenario of thyroid imaging. While a "step and shoot" protocol requires stopping the robot in discrete positions, a continuous movement trajectory would substantially accelerate the data acquisition. We further compare maximum-likelihood expectation–maximization (ML-EM) for time-integrated count values and list-mode expectation–maximization (LM-EM) for individually detected gamma rays. Based on a realistic phantom of the thyroid including hot and cold nodules as well as background radioactivity, we analyze both acquisition protocols in combination with both reconstruction methods. Furthermore,

we statistically subsample the measured data to simulate lower uptakes, thus creating artificial settings of less radioactivity without changing other aspects of the acquired data.

2. RECONSTRUCTION METHODS

2.A. Fundamentals

As a non-negative quantity, the mean number of emissions within the volume $V \subset \mathbb{R}^3$ can be considered a function $f : V \to \mathbb{R}_0^+ = [0,\infty)$, discretized as

$$f(\cdot) \approx \widehat{f}(\cdot) = \sum_{j=1}^{J} x_j b_j(\cdot), \tag{1}$$

with $b_j(\cdot)$ denoting spatial basis functions, in our case isotropic cubic voxels, and $\mathbf{x} = (x_j)_{j=1}^{J}$ representing their respective coefficients — voxel-wise mean number of emissions, so to say. The latter are initially unknown, and will be computed during reconstruction. An approximation of f can later be recovered via Eq. (1). For simplicity, we just use index j to refer to voxel b_j.

Reconstruction itself is based on the observation of nuclear decay events. Following a "preset time" acquisition protocol (rather than "preset counts"), both the *total number of detected emissions N* as well as the individual occurrences are random. In particular, N is a realization of a Poisson distributed random variable with

$$\overline{N} = \sum_{j=1}^{J} x_j d_j \tag{2}$$

denoting its expectation. (For brevity we assume unit measurement times.) d_j is the *detection sensitivity* of voxel j, i.e., the probability that an emission from voxel j was detected or, in other words, a number giving an estimate for how well a voxel is covered during the measurements. Considering our flexible detector, the robotically controlled mini gamma camera, this magnitude can vary noticeably over j.

We use two different recording schemes — *binned-mode* for time-integrated count values and *list-mode* for individually detected emissions. Each of them leads to a specific expectation–maximization algorithm for reconstruction, to be outlined below. In both cases, the detector is moved robotically during acquisition of data, and we mark the different *detector poses* using the index $t \in \{1,\ldots,T\}$.

Furthermore, we need to know the *general measurement probability*

$$P_{tj} := P[\text{emission from voxel } j \text{ detected at detector pose } t] \tag{3}$$

that, for example, can be measured by the systematic long-term observation of the imaging setup. In traditional tomographic reconstruction nomenclature, P can be called *system matrix*, describing the characteristics of the imaging setup independent of actual distributions. We consider it known for now; the calibration procedure[12] is outlined in Sec. 3.B. Note that P relates to independent emissions and is hence valid for all recording modes. Also consider that geometrical information such as

position and orientation of the gamma camera with respect to the volume of interest is indirectly contained within P.

Based on P, it is also possible to give an estimate for the voxel-wise detection sensitivity,

$$d_j = \sum_{t=1}^{T} P_{tj}. \tag{4}$$

Unrelated to actual emissions, d_j contains purely geometrical information only, describing how well voxel j is observed.

2.B. Binned-mode data and maximum-likelihood expectation–maximization (ML-EM)

A common approach is to store counts $y_i \in \mathbb{N}_0 := \{0,1,\dots\}$ of emissions integrated over certain time frames. This corresponds to temporal binning, and may happen natively in the detector hardware or retrospectively in software. The number of detector poses T then equals the number of measured time-integrated counts $\mathbf{y} = (y_i)_{i=1}^{I}$, and we can use the indices t and i interchangeably.

Now we introduce the discrete random variables Y_{ij} as the number of emissions from voxel j detected at a time frame i. We assume, as is typical[16] and experimentally confirmed,[17] that the Y_{ij} are independent and Poisson distributed with mean $P_{ij}x_j$, using the general measurement probability P_{ij} from Eq. (3). Let further the discrete random variables $Y_i = \sum_{j=1}^{J} Y_{ij}$ denote the number of emissions detected at a time frame i. Y_i are then again Poisson distributed with mean

$$(P\mathbf{x})_i := \sum_{j=1}^{J} P_{ij}x_j. \tag{5}$$

Our task is now to estimate $\mathbf{x} = (x_1,\dots,x_J)$ using the *binned-mode data likelihood function*

$$L_{\mathrm{bin}}(\mathbf{x}) = \prod_{i=1}^{I} \exp\left(-(P\mathbf{x})_i\right) \frac{(P\mathbf{x})_i^{y_i}}{y_i!}. \tag{6}$$

Ignoring constants irrelevant to subsequent optimization, the corresponding *binned-mode data log-likelihood function* is

$$\ell_{\mathrm{bin}}(\mathbf{x}) = -\sum_{i=1}^{I} (P\mathbf{x})_i + y_i \log (P\mathbf{x})_i + \mathrm{const}. \tag{7}$$

A well-known algorithm maximizing (7) is the *maximum-likelihood expectation–maximization*[18] (ML-EM), iteratively updating a vector initialized as $\mathbf{x}^{(0)} = \mathbf{1}$ using the following multiplicative update:

$$x_j^{(k+1)} = x_j^k \cdot \frac{1}{d_j} \sum_{i=1}^{I} P_{ij} \frac{y_i}{(P\mathbf{x}^{(k)})_i} \tag{8}$$

for $j = 1,\dots,J$. Here, $d_j = \sum_{i=1}^{I} P_{ij}$ again denotes the voxel-wise detection sensitivity.

2.C. List-mode data and list-mode expectation–maximization (LM-EM)

In general, binning may lead to aliasing artifacts, as additional measurement errors are inherently introduced

during the process, and it may be advisable to treat the original measurements separately. In our case, for instance, the camera will move during the acquisition, thus invalidating the static model implicitly assumed when using time-integrated count values. Therefore, in list-mode recording settings, instead of counts, every individual detected emission (or "event") is stored in a list, and the total number of emissions is N, a realization of the Poisson random variable introduced earlier with mean $\overline{N} = \sum_{j=1}^{J} x_j d_j$ and probability mass function

$$P(N) = \exp(-\overline{N}) \frac{\overline{N}^N}{N!}. \tag{9}$$

Let Z denote the set of all possible emissions, and let $\{z_1,\dots,z_N\} \subset Z$ denote the list of detected emissions. The probability density function for an emission z_n on the list, $n \in \{1,\dots,N\}$, is

$$h(z_n) = \overline{N}^{-1} \cdot \sum_{j=1}^{J} P_{nj}x_j \tag{10}$$

using the general measurement probability P_{nj} from Eq. (3).

Our task is now to estimate $\mathbf{x} = (x_1,\dots,x_J)$ using the *list-mode data likelihood function*

$$L_{\mathrm{list}}(\mathbf{x}) = P(N) \cdot \prod_{n=1}^{N} h(z_n). \tag{11}$$

Again ignoring constants irrelevant to subsequent optimization, the corresponding *list-mode data log-likelihood function* is

$$\ell_{\mathrm{list}}(\mathbf{x}) = -\overline{N} + \sum_{n=1}^{N} \log\left(\sum_{j=1}^{J} P_{nj}x_j\right) + \mathrm{const}. \tag{12}$$

An algorithm maximizing (12) similar to ML-EM has been proposed,[19–21] iteratively updating a vector initialized as $\mathbf{x}^{(0)} = \mathbf{1}$ using the following multiplicative update:

$$x_j^{(k+1)} = x_j^{(k)} \cdot \frac{1}{d_j} \sum_{n=1}^{N} P_{nj} \frac{1}{(P\mathbf{x}^{(k)})_n} \tag{13}$$

for $j = 1,\dots,J$, employing the short-hand notation $(P\mathbf{x})_n := \sum_{j=1}^{J} P_{nj}x_j$. Here, $d_j = \sum_{t=1}^{T} P_{tj}$ again denotes the voxel-wise detection sensitivity, which is dependent only on the detector's trajectory, i.e., the poses $t \in \{1,\dots,T\}$, and on the choice of collimation.

We use the term *list-mode expectation–maximization* (LM-EM) to refer to this method.

3. HARDWARE SETUP

Our experiments aim at comparing different acquisition and reconstruction modes for thyroid imaging using a flexible mini gamma camera setup. In order to have equivalent, realistic data in each of the settings, our setup consists of three components: a custom designed thyroid phantom, a mini gamma camera, and a robotic arm guiding the camera (see Fig. 1).

The mini gamma camera is a Crystal Cam by Crystal Photonics GmbH.[22] The detector of the camera uses CdZnTe

(a)   (b)

FIG. 1. Hardware setup and thyroid phantom. (a) Complete setup with part of the robotic arm (I), gamma camera holder (II), gamma camera (III), and thyroid phantom (IV) and (b) rendering of the thyroid phantom (bottom half). Two medium-sized nodules (I, II) are on the left, a small (III) and a big one (IV) on the right. (See color online version.)

and measures $40 \times 40 \times 5$ mm^3 divided in 16×16 pixels. In front of the detector, there is an 11 mm parallel hole tungsten collimator (one hole per pixel) with lead shielding at the side. The energy resolution is less than 7% at 140 keV. We selected an energy window of $\pm 5\%$ around the 140 keV gamma peak of ^{99m}Tc.

The robot, a Universal Robots[23] UR5 with six degrees of freedom, and the camera are rigidly coupled by a custom-designed adapter. The main purpose of the robot is to have accurate position tracking and reproducible trajectories.

3.A. Phantom

Many commercial phantoms for scintigraphy are intended for planar acquisition only. Our custom-printed phantom is designed to better mimic a human thyroid, both in terms of three-dimensional shape as well as volume. A rendering of the model and a picture of the complete setup are shown in Fig. 1.

The phantom consists of a chamber shaped like a thyroid, with four inner chambers resembling nodules [numbered I to IV as marked in Fig. 1(b)], inside a box-like enclosure.

The phantom is mostly symmetric, with small cylindrical support structures (2 mm diameter) that hold the thyroid and inner chambers in place with respect to the enclosure. The support structures at the top of the phantom have a hole of

0.5 mm diameter that connects the nodule chambers with the outside of the phantom, enabling the user to fill the chambers with a syringe. An additional hollow support structure enables separate filling of the thyroid body and the outer chamber. The outer bottom part of the enclosure is rectangular, while the top part is rounded, to mimic the neck region better.

The total volume of the thyroid (including the inner chambers and the support material) is 15.5 ml and the effective volume is 12.6 ml. The smallest chamber (III) has a volume of 0.11 ml (6 mm inner diameter), the medium sized ones (I, II) 0.27 ml (8 mm inner diameter), and the bigger elongated one (IV) 0.87 ml (8 mm diameter halfspheres connected by a cylinder, with a total length of 20 mm). Figure 2(b) shows a mechanical drawing of the phantom, including the relevant dimensions.

3.B. Calibration and characterization

In order to produce tomographic reconstructions, accurate modeling of the sensors' measurement probabilities P relative to the elements of the discretized volume of interest is essential. For a diagnostic scanner with a fixed camera geometry, these probabilities can be calibrated by exhaustively observing a nuclear source moving within the field of view. For our case of a flexible mini gamma camera, however,

(a)   (b)

FIG. 2. Graphical and mechanical description of the thyroid phantom.(a) Extracted coronal section (in blue), transverse sections (in yellow and red), and profile extraction location (in green) and (b) mechanical drawing. (See color online version.)

this modeling is more complicated and requires a twofold approach: First, a characterization of the static gamma camera, and second, accurate tracking of the camera while moving around the volume of interest.

Its first component, the characterization of the camera, was obtained measuring its response to a ^{57}Co point source while moving it using a positioning table with all three translational degrees of freedom, thus yielding finely sampled lookup tables. The measurements of eleven camera pixels had to be discarded due to faulty responses. A full description of this process is given in an earlier publication.[12]

The second component, accurate tracking, is obtained through forward kinematics of the robotic arm. Its sensors are able to provide better location information at higher sampling rates (0.1 mm and 125 Hz, respectively) compared to optical and electromagnetic systems already used in the operating room.[24]

The camera is attached to the wrist of the robotic arm using a custom-designed, 3D-printed holder. The robot's base coordinate system is also used as the main coordinate system. In order to obtain a complete transformation chain, the transformation from the region of interest to the detector and the measurement probability lookup tables need to be fused. The missing Euclidean transformation from the robot wrist to camera sensor plane can be recovered by measuring the 3D-printed part directly using a caliper.

3.C. Data acquisition

Finally, positions reported by the robot and gamma rays observed by the camera need to be correlated. The robot and the gamma camera are connected to one computer, where each event (robot location update or gamma ray measurement) is recorded and timestamped. In this way we can assign a camera position in space to every detector reading.

4. EXPERIMENT DESIGN

With this setup in place, two datasets have been acquired. The first one consists of a *step and shoot (SAS)-trajectory* around the phantom. In such a setting, the camera is moved to a certain pose, at which measurements are acquired only while the camera remains in place. Afterward, the camera is moved to the next pose to resume measuring there. The second dataset is a *"continuous" trajectory* where the camera is moving smoothly while continuously measuring.

4.A. Datasets

For the SAS case, three parallel half-elliptic trajectories were computed around the phantom, and every 3° over the ellipse, the camera was first positioned perpendicular to the phantom, and then tilted by 30° and −30° as second and third poses, see Fig. 3. We measured three half-ellipses of 61 stopping points each. Considering the three perspectives at every stopping point, the total number of poses amounts to 549 for SAS. At each pose, the acquisition time was 0.6 s, yielding an effective acquisition time of 329 s. The movement
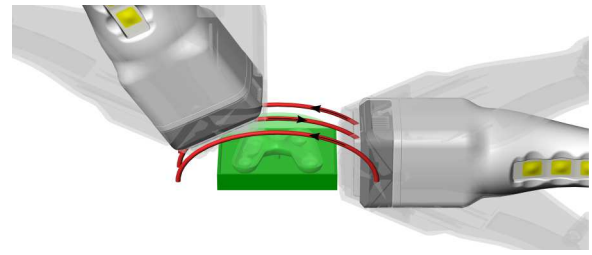

FIG. 3. Rendering of the gamma camera, showing the scanning positions with respect to the phantom (in green). Measurements were acquired at each position along the trajectory (in red) using three tilts at 0° and ±30°, in plane with respect to the trajectory. In total, three half-elliptical movement paths were performed over the thyroid to achieve full coverage. (See color online version.)

of the camera took 654 s in total. We only consider gamma rays detected while the setup is stationary.

For the continuous case, a similar trajectory was generated. However, this time, we were continuously measuring gamma rays during movement without stopping the movement. We used the same ellipses with the same ±30° tilts as basis for the trajectory. The complete continuous trajectory was executed in 293 s.

4.B. Reconstruction

With these two datasets and the two expectation–maximization reconstruction algorithms (cf. Sec. 2), a total of four combinations have been investigated: For *step and shoot ML-EM*, the static poses were extracted, and all respective detections were accumulated into pixel-wise counts, i.e., binned according to poses. For *step and shoot LM-EM*, the same trajectory with static poses was used, and the selected events are identical to the ones used in the previous dataset, but in this case they are represented as a list of events without any binning. For *continuous ML-EM*, the data from the continuous trajectory were temporally binned into intervals of 48 ms, similar to the refresh rate of an optical tracking system[24] as used commercially.[25] For *continuous LM-EM*, we used the continuously acquired detections directly as a list of events.

For all reconstructions, we used a volume of interest of $80 \times 80 \times 50$ mm^3 with 2 mm^3 isotropic cubic voxels.

For all reconstructions, we used 166 iterations of the respective algorithm. This number was selected as the maximum number of iterations such that all experiments achieve a likelihood difference between subsequent iterations of less than $5 \cdot 10^{-6}$.

Additionally, we used a simple attenuation correction built in the system matrix, assuming that the phantom completely consists of water. No scatter correction was used. The reconstructions were postprocessed with an isotropic Gaussian filter with a kernel size of 1 mm^3 (0.5 voxels).

4.C. Radioactivity and simulated lower uptake

The nodules I, III, and IV (hot nodules) were loaded with a solution with the same concentration of ^{99m}Tc, yielding a total of 3 MBq of activity. This solution was then diluted 1:10, and

used to fill the thyroid chamber, resulting in a total activity of 6 MBq for the whole phantom. The outer chamber was filled with water, and nodule II (cold nodule) was left empty.

In our university clinic, the patients receive an injection of 67 MBq on average, and the mean uptake in the thyroid is 1.7%, resulting in approximately 1.1 MBq. In general, the injected value is relatively constant, but the uptake is very patient-dependent. That results in about 10% of the patients having an uptake of less than 300 kBq and about 5% of the patients having an uptake of over 6 MBq.

To understand how the uptake influences the result of the reconstructions, and to better cover the uptake range of patients, simulated lower uptake experiments were performed using the acquisitions with the phantom loaded as described before.

Therefore, we consider two additional virtual settings, 20% of the total activity (equaling 1.2 MBq, approximately the average in our clinic) and 5% (0.3 MBq, a lower bound covering almost 90% of our patients). We employed statistical rejection sampling, using the temporal histogram of the original detections to reject measurements. Thus we produce a temporal histogram with approximately the same shape, but with the amplitude scaled down to the desired acceptance factor.[26] To better understand the effect of the statistical subsampling, we produced multiple noise realizations for each dataset.

In total, we repeated each of the four reconstruction experiments once with the full data (*high uptake*), 16 times with 20% (*medium uptake*) and 16 times with 5% (*low uptake*) of the originally acquired observations.

4.D. Planar scintigraphy

Planar scintigraphy is the current main imaging modality for thyroid diagnosis. To emulate the results of a scintigraphy, which is using a significantly bigger, stationary gamma camera, our camera was positioned orthogonally overlapping 21 positions that were afterward stitched together to generate one full image. At each position, the camera was held for 3 s, the images were upsampled, the results in the overlapping regions were averaged, and the image was downsampled again to 1 mm^2 isotropic pixels.

5. RESULTS

Figure 4 shows the planar scintigraphy of the thyroid phantom acquired using our setup. In comparison, Fig. 5 shows the three-dimensional reconstructions using both ML-EM and LM-EM for the step and shoot (SAS) and the continuous (Cont.) datasets when using all the original detections, i.e., the high uptake data set. The first row shows the equivalent coronal center cross sections through the reconstructed radioactivity distributions. The transverse cross sections shown in the second row are positioned to contain the centers of nodules I and III, and the transverse cross sections in the third row are positioned to show the isthmus connecting both thyroid lobes, above nodules II and IV. The location of the coronal cross section and the two transverse planes with respect to the thyroid phantom is indicated in Fig. 2(a). All intensities are scaled to the interval [0,1] for each reconstruction individually, and the colors are represented in a nonlinear fashion in order to highlight low contrast regions.

As seen in Fig. 5, the two algorithms (ML-EM and LM-EM) yield very similar reconstruction results for the same dataset, extending even to the shape of artifacts. In all settings, the thyroid is reconstructed and hot and cold nodules are discernible. However, the isthmus between the lobes is not reconstructed very well when using the SAS trajectory, erroneously bulging away from the center.

Figure 6 compares the same cross sections for the high uptake data set (6 MBq), one representative simulated medium uptake data set (1.2 MBq, corresponding to the average patient
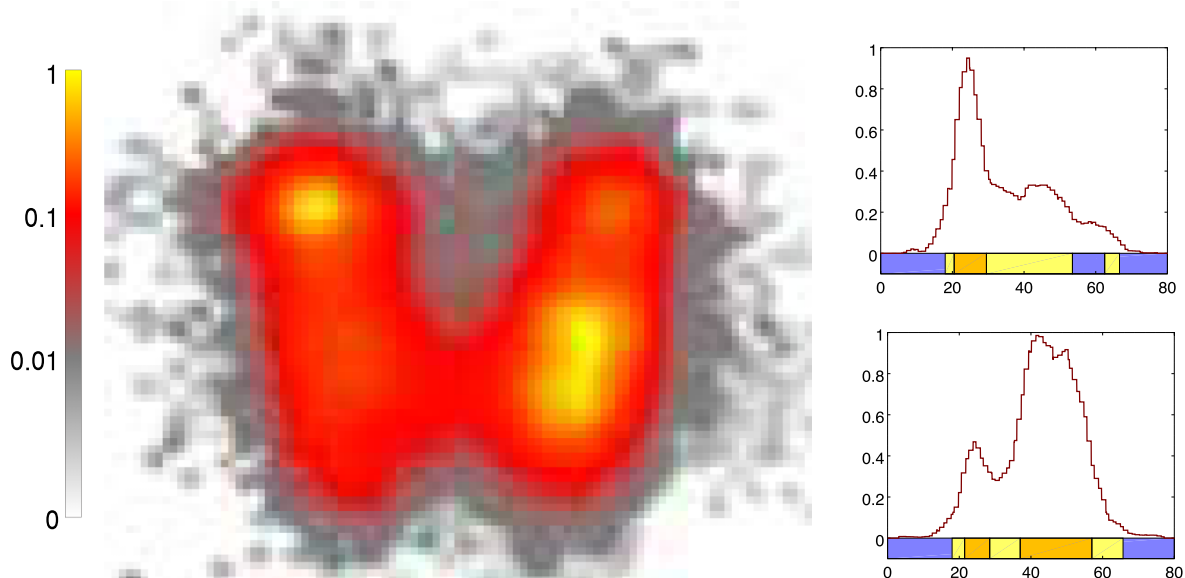

Fig. 4. Planar scintigraphy and line profiles of the thyroid phantom, created using the gamma camera in 21 stationary positions, averaging the overlapping areas. The profiles were extracted from the planar image in a similar fashion as the ones presented in Fig. 7.
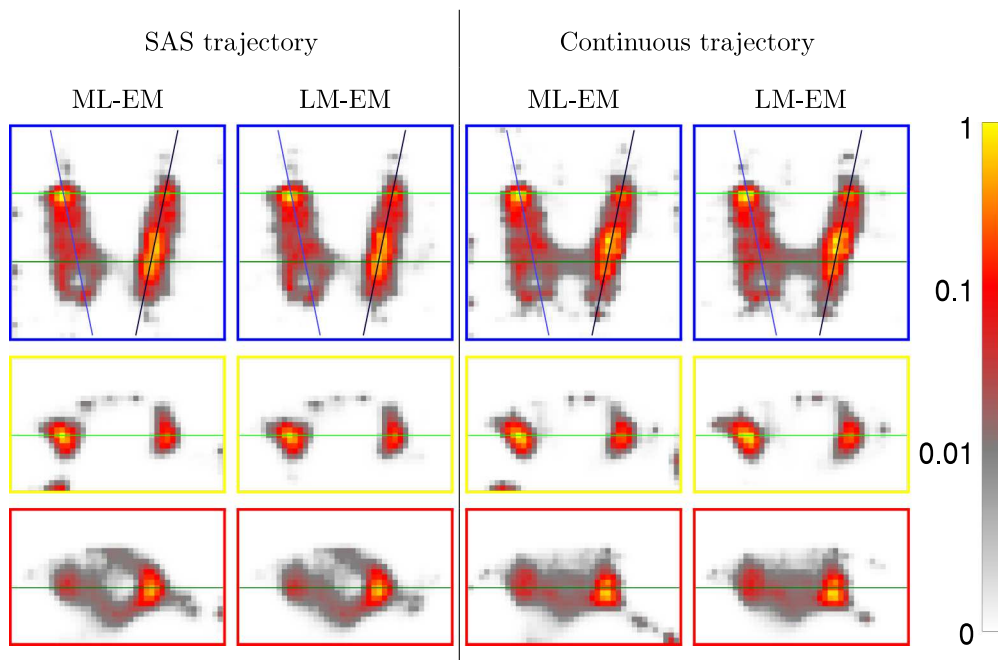
FIG. 5. Reconstruction results of all four methods using the *high uptake* (6 MBq) data set. Shown are coronal cross sections (top row) as well as two transverse cross sections (middle and bottom row). The locations of the cross sections are illustrated in Fig. 2(a). All intensities are scaled to the interval [0, 1] for each reconstruction individually.

in our clinic), and one representative simulated low uptake data set (300 kBq, corresponding to less than 10% of the patients in our clinic regardless of pathology). This time we only show the results using the SAS trajectory and ML-EM reconstruction as well as the continuous trajectory and LM-EM reconstruction, as these are the only practically relevant methods.

With decreasing uptake the image quality deteriorates as expected. In particular, for both methods the reconstruction of the thyroid background loses homogeneity with decreasing uptake, while maintaining the overall characteristics as described for the high-uptake experiments.

Figure 7 shows line profiles extending in the sagittal direction through the nodules in both the left and right lobes of the thyroid phantom, respectively. The profile in the left lobe passes through the centers of nodules I and II and the profile in the right lobe passes through the centers of nodules III and IV, as indicated in Fig. 2(a). For reconstructions using the SAS trajectory and ML-EM, the profiles are marked in red, and for
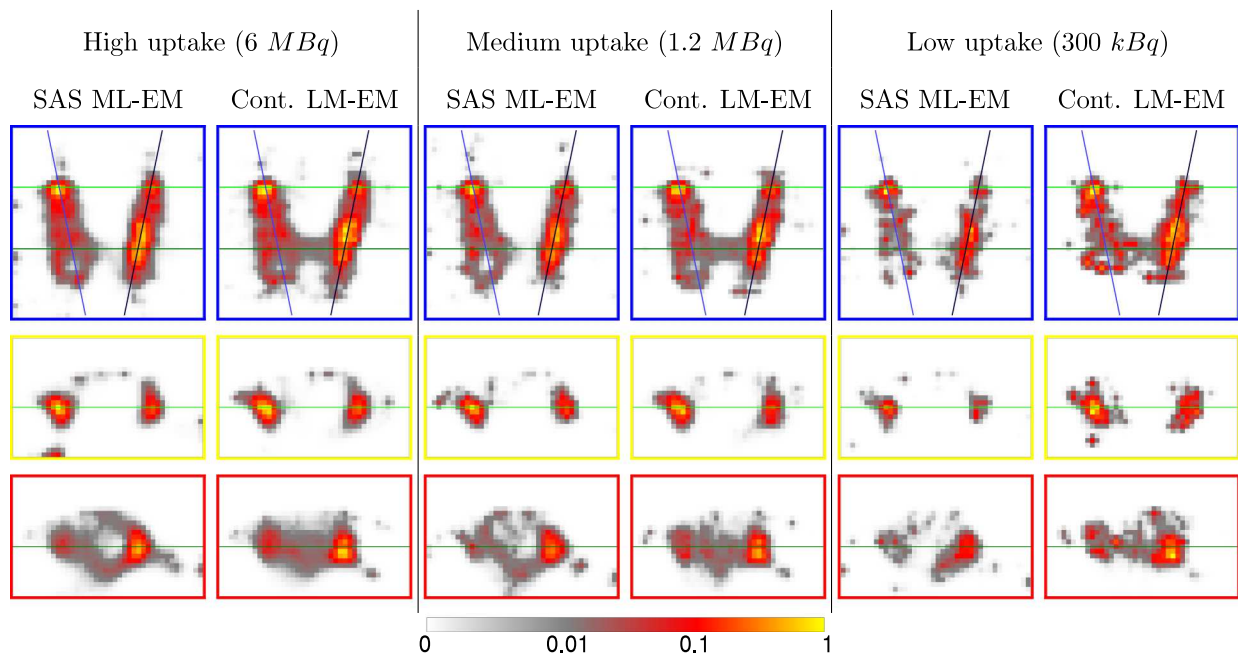

FIG. 6. Reconstruction results of data sets with high, medium, and low uptakes using the SAS trajectory and ML-EM (left columns) and the continuous trajectory and LM-EM (right columns). Shown are coronal cross sections (top row) as well as two transverse cross sections (middle and bottom row). The locations of the cross sections are illustrated in Fig. 2(a). All intensities are scaled to the interval [0, 1] for each reconstruction individually.
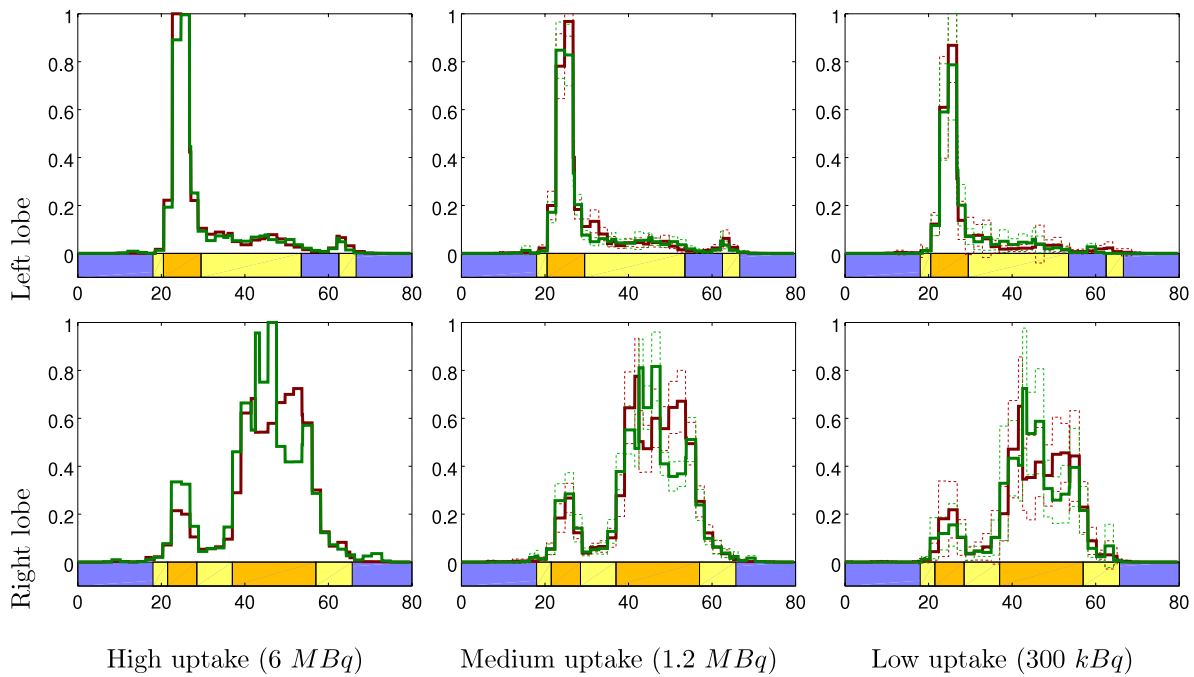
FIG. 7. Profile plots for the reconstructions computed from high, medium, and low uptake data. For the medium and low uptakes, the plot shows the average value of the realizations, and the dotted profiles correspond to one standard deviation away from the mean. The profiles for the reconstructions using SAS trajectory and ML-EM are shown in *red*, the ones using continuous trajectory and LM-EM are shown in *green*. The ground truth is shown as a colored bar below the profile; *orange* for 100% activity (hot nodules), *light yellow* for 10% activity (background), and *blue* for 0% (cold nodule and areas outside the phantom). The profile in the left lobe passes through the centers of nodules I and II and the profile in the right lobe passes through the centers of nodules III and IV, as indicated in Fig. 2(a). (See color online version.)

reconstructions using the continuous trajectory and LM-EM, the profiles are marked in green.

Numerical magnitudes for quantitative comparison are given in Fig. 8 for all experiments. The contrast recovery coefficient (CRC) is presented for each nodule, calculated as $(c_{r1}/c_{r2}-1)/(c_1/c_2-1)$, where c_{r1} is the mean concentration at the nodule location, c_{r2} is the mean value of the background, and c_1/c_2 is the ground truth ratio between them. In the perfect case, the CRC has a value of 1, a value smaller or bigger than 1 indicates under- or over-estimation, respectively.

In detail, the CRC was calculated using the following procedure: The location of each nodule was extracted from the phantom's drawings, and then used to select the corresponding voxels from the reconstruction, minus a small border (0.5 voxels, or 1 mm). c_{r1} is then computed as the average activity of these voxels, where partially selected voxels at

the borders were weighted accordingly. To obtain the mean background activity c_{r2}, two spheres of the same size as the medium nodules were extracted on each side of the thyroid, where it was certain that the area belonged to the background, and then the contained activity was averaged.

In general, for high uptake, the four combinations of the two datasets and the two reconstruction algorithms yield very similar results: The CRC of the large hot nodule IV is overestimated (as being too radioactive), and the ratios of all other nodules are slightly underestimated. For medium uptake, ML-EM SAS also overestimates the ratio of the more separate hot nodule I. For low uptake, the results are somewhat more diverse, and in particular, the large hot nodule IV is overestimated in all cases. Comparing all settings, the CRC of cold nodule II is always underestimated, i.e., reconstructed to be more radioactive than in reality.
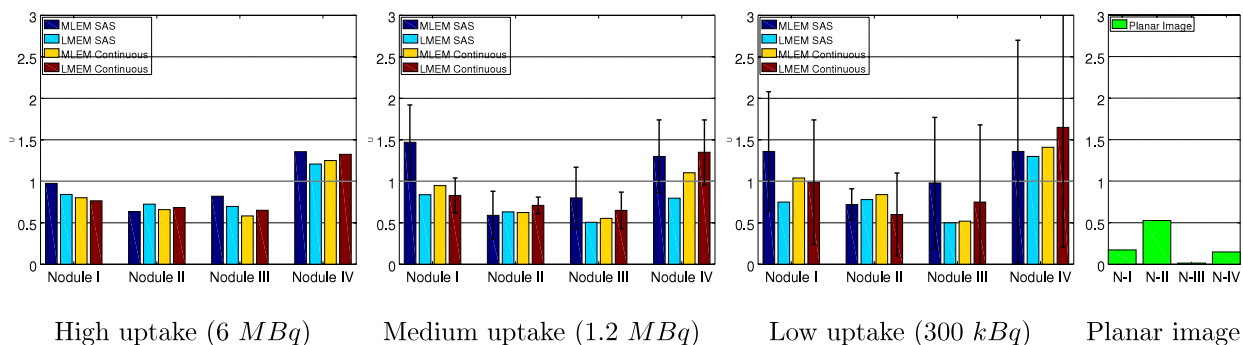

FIG. 8. Contrast recovery coefficients for nodules I–IV in the thyroid phantom, computed for each of the four reconstruction methods using the high, medium, and low uptake data sets. As comparison, the contrast recovery coefficients obtained from the planar image are presented on the right.

TABLE I. Time required (in seconds) for trajectory execution as well as number of detected emissions for each experiment. Additionally, average time required (in seconds) for one iteration of the reconstruction algorithms (ML-EM and LM-EM) for each experiment.

Data set	High uptake		Medium uptake		Low uptake	
Trajectory	SAS	Cont.	SAS	Cont.	SAS	Cont.
Trajectory execution (s)	654	293	654	293	654	293
Detected emissions	323 859	313 671	65 056	63 352	16 358	15 725
ML-EM iteration (s)	34	459	34	454	35	453
LM-EM iteration (s)	140	146	42	43	12	13

Finally, Table I provides the time required for trajectory execution and the number of detected emissions for each experiment. In addition to these values, the average time required to perform one iteration of the reconstruction algorithm is specified (a total of 166 iterations was performed for each reconstruction), using our own custom software package executed on a dual Intel Xeon (E5-2687W) machine with 64 GB of RAM.

6. DISCUSSION

In our experiments we compare two acquisition protocols, step-and-shoot (SAS) and continuous, together with two reconstruction methods, binned-data ML-EM and list-mode LM-EM. While the SAS trajectory lends itself quite well to binned-data ML-EM, and conversely the list-mode LM-EM fits perfectly to the continuous trajectory, the two other combinations SAS/LM-EM and continuous/ML-EM are feasible as well and produce reconstructions with very similar characteristics overall: As shown in Fig. 5 for the high uptake data, all three hot nodules are clearly visible in all four methods, and it is also possible to infer the cold nodule with each method. The contrast recovery coefficients for the same data set are also fairly consistent across all four methods, as seen in the left column of Fig. 8. Compared to the planar image in Fig. 4, the cold nodule visibility is the biggest improvement in the reconstructions. Additionally, the continuous trajectory reconstructions resolve the isthmus between the two lobes of the thyroid phantom better, yielding a significantly more accurate representation of that area. We hypothesize that this is caused by the increased coverage of the central area, as the gamma camera sensor, which is too small to image the entire isthmus area at once, can acquire more different view points while continuously moving as opposed to the few viewpoints acquired by the SAS trajectory.

For the data set with medium uptake (middle columns of Figs. 6 and 8), the outcome is similar to the one of the high uptake data, but slightly more noise is visible in the images, as expected from the reduction of counts. In fact, for all noise realizations, the standard deviation of the background activity increases by 74% compared to the high uptake data. The four nodules are qualitatively recovered clearly, including the cold nodule. The corresponding CRC values of all nodules are very

close to the high uptake values, with the exception of SAS ML-EM, which is now markedly overestimating nodule I.

In the low uptake results (right columns of Figs. 6 and 8), the noise is even more dominant. Over all noise realizations, the standard deviation of the background activity now increases by 109% compared to the high uptake data. Qualitatively, the cross-sectional images shown no longer allow a clear determination of which regions represent cold and hot nodules, except for the big nodule IV, which is still visible. When taking into account the full three-dimensional reconstructed image, however, nodule I and nodule II (the cold nodule) can be inferred, for example, from the line profiles, see Fig. 7. This is also reflected by the CRC values in Fig. 8. Since the background values in these images are close to zero, the calculation of the contrast values is dominated by these regions, explaining the highly overestimated values, in particular for nodule IV.

In terms of measurement time (see Table I), the continuous trajectory is clearly preferable, as it allows continuous movement while acquiring data. In our example, actual measurement time was cut in half compared to SAS, while still offering comparable detection statistics.

In terms of computational effort (see again Table I), the combination of SAS trajectory and binned-data MLEM performs very fast, as there is a limited number of static detection poses, and computational complexity is roughly proportional to this number. While the combination of SAS and list-mode LM-EM is feasible, yielding comparable image quality, there is a big drawback in terms of computational effort, except for the case of very low detection statistics. When using the continuous trajectory, the combination with binned-data MLEM is again feasible, yielding comparable image quality, but due to the huge number of bins required to accurately represent the data of the moving detector, the computational effort for reconstruction is needlessly high. The LM-EM method is clearly the better choice for continuously acquired data. It results in fast reconstruction times, and since the computational effort is bound to the number of events and not camera poses, it can also result in reconstruction times faster than SAS ML-EM for low uptakes.

In general, all four presented methods are suitable for mini gamma reconstructions of the proposed thyroid phantom. However, the continuous trajectory achieves a better coverage of the phantom, resulting in better resolved images in the center region of the phantom, while also providing significantly faster acquisition speeds. Meanwhile, for continuous trajectories, the LM-EM reconstruction method is a natural fit, yielding comparable images to ML-EM but significantly faster reconstruction times.

Overall, our proposed approach using mini gamma cameras for three-dimensional imaging provides image quality between scintigraphy and SPECT, while allowing significantly faster acquisition times. In particular, our proposed approach is more easily affordable and enables the visualization of cold nodules, as demonstrated in case of our thyroid phantom.

We note that the field of view of the mini gamma camera is limited and usually cannot cover the entire region of interest at once. As a result, additional uptake, such as in salivary glands, might be in the field of view only for some of the

recorded view points, potentially leading to artifacts in the reconstructed image.

Another important point to consider for clinical implementation is the tracking and guidance of the camera. One option is to remove the robot, to add a tracking system of sufficient accuracy for localization of the detector, such as outside-in Ref. 24 or inside-out Ref. 27 tracking, and to leave the movement of the camera entirely to a human operator. This approach is currently used in radio-guided surgery on an open situs.[10,11] Naturally, this implies a continuous trajectory and list-mode data LM-EM reconstruction. The main disadvantage of the hand-held approach is the loss of repeatability and the weight of the gamma camera that has to be borne by the human operator.

While using a robotic arm eliminates these disadvantages, it requires developments to ensure the required safety for patient applications. Collaborative medical robotic systems that interact with a human operator in order to provide nuclear imaging in addition to ultrasound,[28] or that can autonomously acquire ultrasound images on human probands[29] are a precursor for the wider introduction of robotic imaging. Additionally, a robot enables the incorporation of optimized trajectories based on the scanning geometry[30] to even further reduce acquisition times. A more elaborate option is acquisition optimization schemata, where, for example, the robot adjusts the scanning speed to provide a simultaneously good spatial coverage and good detection statistics, generating patient-specific scans. Robotic nuclear imaging systems could find their application in real-time imaging of the radioactivity distribution during radioembolization of the liver,[13] or the application of radioguidance to laparoscopic surgeries.[31]

7. CONCLUSION

In this work, we have presented two different acquisition modes, step-and-shoot and continuous mode, combined with two reconstruction methods, binned-mode ML-EM and list-mode LM-EM, for mini gamma camera imaging of a thyroid phantom. The combination of continuous trajectory and LM-EM emerged as the clear favorite, due to improved coverage and both fast acquisition and reconstruction times. Finally, continuous trajectories enable practical clinical scenarios, with and without a robot.

ACKNOWLEDGMENTS

CONFLICT OF INTEREST DISCLOSURE

The authors have no COI to report.

a)Now at Paul Scherrer Institut, Villigen, Switzerland.
b)Electronic mail: lasser@in.tum.de

1J. Ferlay, E. Steliarova-Foucher, J. Lortet-Tieulent, S. Rosso, J. Coebergh, H. Comber, D. Forman, and F. Bray, "Cancer incidence and mortality patterns in Europe: Estimates for 40 countries in 2012," Eur. J. Cancer **49**, 1374–1403 (2013).
2A. Jemal, R. Siegel, J. Xu, and E. Ward, "Cancer statistics, 2010," Ca-Cancer J. Clin. **60**, 277–300 (2010).
3L. Davies and H. Welch, "Increasing incidence of thyroid cancer in the United States, 1973-2002," J. Am. Med. Assoc. **295**, 2164–2167 (2006).
4L. Leenhardt, P. Grosclaude, and L. Chérié-Challine, "Increased incidence of thyroid carcinoma in France: A true epidemic or thyroid nodule management effects? Report from the French Thyroid Cancer Committee," Thyroid **14**, 1056–1060 (2004).
5E. P. Simard, E. M. Ward, R. Siegel, and A. Jemal, "Cancers with increasing incidence trends in the United States: 1999 through 2008," Ca-Cancer J. Clin. **62**, 118–128 (2012).
6B. Haugen, E. Alexander, K. Bible, G. Doherty, S. Mandel, Y. Nikiforov, F. Pacini, G. Randolph, A. Sawka, M. Schlumberger, K. Schuff, S. Sherman, J. Sosa, D. Steward, R. Tuttle, and L. Wartofsky, "2015 american thyroid association management guidelines for adult patients with thyroid nodules and differentiated thyroid cancer: The american thyroid association guidelines task force on thyroid nodules and differentiated thyroid cancer," Thyroid **26**, 1–133 (2016).
7U. Y. Ryo, P. V. Vaidya, A. B. Schneider, C. Bekerman, and S. M. Pinsky, "Thyroid imaging agents - A comparison of I-123 and Tc-99m Pertechnetate," Radiology **148**, 819–822 (1983).
8Y. Maruoka, K. Abe, S. Baba, T. Isoda, H. Sawamoto, Y. Tanabe, M. Sasaki, and H. Honda, "Incremental diagnostic value of SPECT/CT with 131I scintigraphy after radioiodine therapy in patients with well-differentiated thyroid carcinoma," Radiology **265**, 902–909 (2012).
9D. Moka, E. Voth, M. Dietlein, A. Larena-Avellaneda, and H. Schicha, "Technetium 99m-MIBI-SPECT: A highly sensitive diagnostic tool for localization of parathyroid adenomas," Surgery **128**, 29–35 (2014).
10T. Wendler, K. Herrmann, A. Schnelzer, T. Lasser, J. Traub, O. Kutter, A. Ehlerding, K. Scheidhauer, T. Schuster, M. Kiechle, M. Schwaiger, N. Navab, S. I. Ziegler, and A. K. Buck, "First demonstration of 3-D lymphatic mapping in breast cancer using freehand SPECT," Eur. J. Nucl. Med. Mol. Imaging **37**, 1452–1461 (2010).
11T. Maurer *et al.*, "Prostate-specific membrane antigen–radioguided surgery for metastatic lymph nodes in prostate cancer," Eur. Urol. **68**, 530–534 (2015).
12P. Matthies, J. Gardiazabal, A. Okur, J. Vogel, M. Friebe, T. Lasser, and N. Navab, "Mini gamma cameras for intra-operative nuclear tomographic reconstruction," Med. Image Anal. **18**, 1329–1336 (2014).
13J. Gardiazabal, M. Esposito, P. Matthies, A. Okur, J. Vogel, S. Kraft, B. Frisch, T. Lasser, and N. Navab, "Towards personalized interventional spect-ct imaging," in *International Conference on Medical Image Computing and Computer-Assisted Intervention* (Springer, Switzerland, 2014), pp. 504–511.
14L. Bouwens, R. Van de Walle, H. Gifford, M. King, I. Lemahieu, and R. Dierckx, "LMIRA: List-mode iterative reconstruction algorithm for SPECT," IEEE Trans. Nucl. Sci. **48**, 1364–1370 (2001).
15A. K. Jha, H. H. Barrett, E. C. Frey, E. Clarkson, L. Caucci, and M. A. Kupinski, "Singular value decomposition for photon-processing nuclear imaging systems and applications for reconstruction and computing null functions," Phys. Med. Biol. **60**, 7359–7385 (2015).
16*Radiological Imaging: The Theory of Image Formation, Detection, and Processing*, edited by H. H. Barrett and W. Swindell (Academic Press, Inc., San Diego, CA, 1981), Chap. 3, p. 98.
17F. Cannizzaro, G. Greco, S. Rizzo, and E. Sinagra, "Results of the measurements carried out in order to verify the validity of the Poisson-exponential distribution in radioactive decay events," Int. J. Appl. Radiat. Isot. **29**, 649–652 (1978).
18L. A. Shepp and Y. Vardi, "Maximum likelihood reconstruction for emission tomography," Trans. Med. Imaging **1**, 113–122 (1982).
19L. Parra and H. H. Barrett, "List-Mode likelihood: EM algorithm and image quality estimation demonstrated on 2-D PET," IEEE Trans. Med. Imaging **7**, 228–235 (1998).
20R. H. Huesman, G. J. Klein, W. W. Moses, J. Qi, B. W. Reutter, and P. R. G. Virador, "List-mode maximum-likelihood reconstruction applied to positron emission mammography (PEM) with irregular sampling," IEEE Trans. Med. Imaging **19**, 532–537 (2000).
21C. Byrne, "Likelihood maximization for list-mode emission tomographic image reconstruction," IEEE Trans. Med. Imaging **20**, 1084–1092 (2001).
22See http://www.crystal-photonics.com for Crystal Photonics GmbH.

[23]See http://www.universal-robots.com for Universal Robots A/S.

[24]See http://www.ndigital.com/medical/products/polaris-family/ for Northern Digital, Inc..

[25]See http://www.surgiceye.com for SurgicEye GmbH.

[26]*Monte Carlo Statistical Methods*, edited by C. P. Robert and G. Casella (Springer Science + Business Media, New York, 2004), pp. 47–51.

[27]P. Matthies, B. Frisch, J. Vogel, T. Lasser, M. Friebe, and N. Navab, "Inside-out tracking for flexible hand-held nuclear tomographic imaging," in *IEEE Nuclear Science Symposium* (IEEE, San Diego, CA, 2015).

[28]M. Esposito, B. Busam, C. Hennersperger, J. Rackerseder, A. Lu, N. Navab, and B. Frisch, "Cooperative robotic gamma imaging: Enhancing US-guided needle biopsy," in *International Conference on Medical Image Computing and Computer-Assisted Intervention* (Springer, Switzerland, 2015), pp. 611–618.

[29]S. Virga, O. Zettinig, M. Esposito, K. Pfister, B. Frisch, T. Neff, N. Navab, and C. Hennersperger, "Automatic force-compliant robotic ultrasound screening of abdominal aortic aneurysms," in *IEEE/RSJ 2016 International Conference on Intelligent Robots and Systems (IROS 2016)* (IEEE, Daejeon, Korea, 2016).

[30]J. Vogel, T. Lasser, J. Gardiazabal, and N. Navab, "Trajectory optimization for intra-operative nuclear tomographic imaging," Med. Image Anal. **17**, 723–731 (2013).

[31]B. Fuerst *et al.*, "First robotic SPECT for minimally invasive sentinel lymph node mapping," IEEE Trans. Med. Imaging **35**, 830–838 (2016).